

**Spatial and radiometric characterization of multi-spectrum
satellite images through multifractal analysis**

Carmelo Alonso^{1,2}, Ana M. Tarquis^{2,3}, Ignacio Zúñiga⁴ and Rosa M. Benito²

¹Earth Observation Systems, Indra Sistemas S.A., Madrid, Spain.

²Grupo de Sistemas Complejos, U.P.M, Madrid, Spain.

³CEIGRAM, E.T.S.I.A.A.B., U.P.M, Madrid, Spain.

⁴Dpt. Física Fundamental, Facultad de Ciencias, Universidad Nacional de Educación a
Distancia (UNED), Madrid, Spain.

Corresponding author: Ana M. Tarquis (anamaria.tarquis@upm.es)

Spatial and radiometric characterization of multi-spectrum satellite images through multifractal analysis

Abstract: Several studies point out that vegetation indexes can be used to estimate root zone soil moisture and earth surface images, obtained by high resolution satellites, give presently huge information on these indexes based in several wavelengths data. Because of the potential capacity for systematic observations at various scales, remote sensing technology extends possible data archives from present time to over several decades back. For this advantage, enormous efforts have been made by researchers and application specialists to delineate vegetation indexes from local scale to global scale by applying remote sensing imagery.

In this work, four bands images have been considered, involved in these vegetation indexes, taken by satellites Ikonos-2 and Landsat-7 of the same geographic location to study the effect of both spatial (pixel size) and radiometric (number of bits coding the image) resolution on these wavelength bands as well as two vegetation indexes: the Normalized Difference Vegetation Index (NDVI) and the Enhanced Vegetation Index (EVI).

In order to do so, a multifractal analysis of these multi-spectral images was applied in each of these bands and the two indexes derived. The results showed that spatial resolution has a similar scaling effect in the four bands, but radiometric resolution has a larger influence in Blue and Green bands than in Red and Near InfraRed bands. The NDVI showed a higher sensitivity to the radiometric resolution than EVI. Both were equally affected by the spatial resolution.

From both factors, the spatial resolution has a major impact in the multifractal spectrum for all the bands and the vegetation indexes. This information should be taken in to account when vegetation indexes based on different satellite sensors are obtained.

Keywords: vegetation index, wavelengths pattern, multifractal spectrum

1 Introduction

Soil moisture is a critical condition affecting interaction of land surface and atmosphere. Remotely sensed data is an important source of information and it can indirectly measure soil moisture in space and time. However, the signal only penetrates the top few centimeters, and soil moisture at deeper layers must be estimated. One method to estimate soil moisture at deeper layers is through vegetation indices. Several authors have investigating the potential of vegetation indices to estimate root zone soil moisture. The Normalized Difference Vegetation Index (NDVI) and Enhanced Vegetation Index (EVI) have been used by several authors (Wang et al., 2007; Ben-Ze'ev et al., 2006; Deng et al., 2007) in different conditions finding significant estimations with root zone soil moisture. For the estimation of these indexes NIR, Red and Blue wavelengths are needed (Huete et al., 2014).

The images provided by the satellites show the land surface in a wide range of wavelengths (from visible to thermal infrared or microwaves) and also with a great variety of spatial resolutions (from a few kilometres to tens of centimetres). The analysis of these varied images and their synergic possibilities are a challenging problem especially with new sensors, which have small spatial resolution and a large range of radiometric quantification. Fractal analysis offers significant potential for improvement in the measurement and analysis of spatially and radiometrically complex remote sensing data. This analysis also provides quantitative insight on the spatial complexity in the information of the landscape contained within these data.

In the general mathematical framework of fractal geometry many analytical methods have been developed; to name a few: textural homogeneity has been characterized using the fractal dimension (Fioravanti, 1994); it has also been used as a spatial measure for describing the complexity of remote sensing imagery (Lam and De Cola, 1993); changes in the image complexity have been detected through the spectral range of hyperspectral images affecting the fractal dimension (Qiu et al. 1999); similarly De Cola (1989) and Lam (1990) have found that fractal dimension also depends on the spectral bands of Landsat-7 TM imagery.

Motivated by the fractal geometry of sets (Mandelbrot, 1983), the development of multifractal theory, introduced in the context of turbulence, has been applied in many areas such as earthquake distribution analysis (Hirata and Imoto, 1991), soil pore characterization (Kravchenko et al. 1999; Tarquis et al. 2003), image analysis (Sánchez et al. 1992) or remote sensing (Tessier et al., 1993; Cheng and Agterberg, 1996; Schmitt et al., 1997; Laferrière and Gaonac'h, 1999; Cheng, 1999; Lovejoy et al., 2001b; Du and Yeo, 2002; Parrinello and Vaughan, 2002; Harvey et al., 2002; Turiel et al. 2005).

The acquisition of remotely sensed multiple spectral images is thus a unique source of data for determining the scale invariant characteristics of the radiance fields related to many factors, such as soil and bedrock chemical composition, humidity content and surface temperature (e.g., Laferrière and Gaonac'h, 1999; Maitre and Pinciroli, 1999; Lovejoy et al., 2001a, b; Harvey et al., 2002; Beaulieu and Gaonac'h, 2002; Gaonac'h et al., 2003). In one of the scheme used in the multifractal analysis, the satellite image is considered as a mass distribution of a statistical measure on the space domain studied and it is analyzed through a multifractal (MF) spectrum (Cheng, 2004; Mao-Gui Hu, 2009; Tarquis et al., 2014), which gives either geometrical or probabilistic information about the pixels distribution with the same singularity. Another technique focus its attention in the variations of a measure analyzing the moments of the absolute differences of their values at different scales, the Generalized Structure Function and the Universal Multifractal model (Lovejoy et al., 2001, 2008; Renosh et al., 2015)

The aim of this work is to characterize by MF analysis the image patterns in the wavelength ranges used for NDVI, EVI and Green bands as well as both vegetation indexes. In order to investigate how the image information is affected by the sampling with different spatial and radiometric resolutions, we have also analyzed images of the same site but acquired by two different satellites: Landsat-7 and Ikonos-2.

We present a comparative analysis of multifractal (MF) tools applied to multi-spectral images obtained by Ikonos-2 and LANDSAT-7. Both satellites have several bands in visible and near-infrared spectral regions in common that can be used in vegetation indexes estimation.

However the bands have different spatial resolution, 4 m for Ikonos-2 and 30 m for LANDSAT-7, and radiometric resolution, 11 and 8 bits respectively. The bands we have chosen are Red (R), Green (G), Blue (B) and Near InfraRed (NIR). For each of those bands, the MF spectrum has been calculated directly from the Hölder exponents α and the singularities spectrum $f(\alpha)$. The same calculations were applied for NDVI and EVI estimated on R, B and NIR bands for each image.

2 Materials and methods

2.1 Images

As already noted, in this work we have analysed two images of the same site acquired from different satellites, Landsat-7 and Ikonos-2. Both are multi-spectral images with several bands that cover several regions of the electromagnetic spectrum in the visible and near infrared wavelength.

Landsat-7 was put in orbits in April 1999. This satellite follows a sun-synchronous orbits at 705 km of altitude, with an equatorial crossing time of 10:00 a.m. in the descending node. It requires 98.8 min to circle the Earth, tracing a worldwide reference system (WRS) of just over 230 ground paths. During at least three decades Landsat-7 orbits over each of these paths once every 16 days in a repetitive cycle (Mika, 1997).

The main Landsat-7 sensor for Earth observation is the Enhanced Thematic Mapper Plus (ETM+). The ETM+ operates as a whiskbroom scanner and acquires data for seven spectral bands: visible (ETM+#1, from 0.45 to 0.52 μm ; ETM+#2, from 0.53 to 0.61 μm ; ETM+#3, from 0.63 to 0.69 μm), near infrared (ETM+#4, from 0.78 to 0.9 μm), shortwave infrared (ETM+#5, from 1.55 to 1.75 μm , and ETM+#7, from 2.09 to 2.35 μm) and thermal infrared (ETM+#6, from 10.4 to 12.5 μm). The ETM+ ground sampling distance (pixel size in the images) is 30 m for the six reflective bands and 60 m for the thermal band. The ETM+ also acquires images for a panchromatic band (ETM+#8, from 0.52 to 0.9 μm) with a 15 m ground sampling distance. The radiometric resolution of the Landsat-7 data is 8 bit/pixel or 256 grey levels for the pixel digital value.

1
2 Ikonos-2 was launched in September 1999. Its panchromatic sensor, with a resolution of 0.82
3 m, provided the first very high resolution images of the Earth's surface from EOS. The
4 Ikonos-2 orbits altitude is approximately 681 km, it is inclined 98.1 degrees to the equator and
5 it provides sun-synchronous operation. The equatorial crossing time of Ikonos-2 is 10:30 am
6 in the descending node. The orbits provides daily access to sites within 45 degrees of nadir
7 (Dial et al. 2003).

8
9 The multi-spectral sensor simultaneously collects blue (IK#1, from 0.445 to 0.516 μm), green
10 (IK#2, from 0.506 to 0.595 μm), red (IK#3, from 0.632 to 0.698 μm) and near infrared (IK#4,
11 from 0.757 to 0.853 μm) bands with 3.28 meter resolution at nadir. Both images,
12 panchromatic and multi-spectral, have a radiometric resolution of 11 bits/pixel or 2048 grey
13 levels for the pixel digital value.

14
15 The Landsat-7 multi-spectral image used in this study was acquired on August 6th 2000 at
16 10:46 a.m. and it corresponds to the scene with WRS coordinates, path and row: 201 - 32.
17 This scene is located in the central region of Spain and it covers a square surface of
18 approximately 180 km side-length, located around Madrid. Solar azimuth and elevation
19 angles for this scene are 132.44 and 58.62 degrees respectively.

20
21 The Ikonos-2 data used in this study is a multi-spectral image acquired on August 8th 2000 at
22 11:03 a.m. It covers a square area of 11 km side located near Aranjuez, south of Madrid, in
23 the central region of Spain. Solar azimuth and elevation angles for this scene are 139.5 and
24 60.79 degrees respectively. Both images were corrected geometrically to the same
25 cartographic projection: UTM, zone 30 N by a co-registration process.

26
27 The analysis has been carried out on a subset that covers (approximately) the same area in
28 both the Landsat-7 and the Ikonos-2 images, corresponding to a region located north the town
29 of Aranjuez. The representative elements of the land used in the selected area are: irrigate
30 crops, pastures, heaths, unirrigated land cultivations and olive groves. The Landsat-7 subset

image is a square of 512 x 512 pixels with a size of 30 m covering a somewhat larger surface than the Ikonos-2 image. The Ikonos-2 image consists of a square subset with 2048 x 2048 pixels and 4 m resolution.

2.2 Vegetation indexes

Vegetation is one of the landscape's elements that have received most attention in the field of image analysis. Therefore, there are many parameters that can be used to obtain information on vegetation from remote sensing imagery.

One of the main parameters are the so-called vegetation indexes. These indices allow to detect the presence of vegetation in an area and its activity, since its values are related to this activity. For this, we can use the reflectance values corresponding to the different wavelengths, interpreting these in relation to the photosynthetic activity. Of these indices, the most commonly used is the Normalized Difference Vegetation Index.

The Normalized Difference Vegetation Index is defined by

$$NDVI = \frac{NIR - R}{NIR + R} \quad (1)$$

where NIR is the pixel value in the near infrared band and R the pixel value in the red band. The values of this index are within the range (-1, 1) and their positive values are sensitive to the proportion of soil and vegetation in each pixel (Carlson and Ripley, 1997). Pixels with $NDVI < 0.2$ are considered without vegetation or bare soil. Pixels with $NDVI > 0.5$ are considered as fully covered by vegetation.

Other vegetation index is called Enhanced Vegetation Index. It is defined by

$$EVI = 2.5 \frac{(NIR - R)}{(L + NIR + C_1 R - C_2 B)} \quad (2)$$

where NIR is the pixel value in the near infrared band, R the pixel value in the red band and B the pixel value in the blue band. L , C_1 and C_2 are constants with the values 1, 6 and 7.5 respectively. The main characteristic of this index is that it corrects some distortions caused by the light dispersion from aerosols, as well as the background soil (Huete et al., 2014).

2.3 Multifractal image analysis

A monofractal object can be measured by counting the number N of δ size boxes needed to cover the object. The measure depends on the box size as

$$N(\delta) \propto \delta^{-D_0} \quad (3)$$

where

$$D_0 = \lim_{\delta \rightarrow 0} \frac{\log N(\delta)}{\log \frac{1}{\delta}} \quad (4)$$

is the fractal dimension. D_0 is calculated from slope of a log-log plot. However, many examples are found where a single scaling law cannot be applied and it is necessary to do a multiscaling analysis.

There are several methods for implementing multifractal analysis. The Universal Multifractal (UM) model assumes that multifractals are generated from a random variable with an exponentiated extreme Levy distribution (Lavallée et al., 1991; Tessier et al., 1993). In UM analysis, the scaling exponent $K(q)$ is highly relevant. This function for the moments q of a cascade conserved process is obtained according to Schertzer and Lovejoy (1987) as follows:

$$K(q) = \begin{cases} \frac{C_2(q^{\alpha_L} - q)}{\alpha_L - 1} & \text{if } \alpha_L \neq 1 \\ C_1 q \log(q) & \text{if } \alpha_L = 1 \end{cases} \quad (5)$$

where C_1 is the mean intermittency codimension and α_L is the Levy index. These are known as the UM parameters.

Other method is the moment method developed by Halsey et al. (1986) and applied to this case study. This method uses mainly three functions: $\tau(q)$, known as the mass exponent function, α , the coarse Hölder exponent, and $f(\alpha)$, multifractal spectrum. A measure (or field), defined in two-dimensional image embedding space ($n \times n$ pixels) and with values based on grey tones (for 8 bits goes from 0 to 255), cannot be consider as a geometrical set and therefore cannot be characterized by a single fractal dimension.

To characterize the scaling property of a variable measured on the spatial domain of the studied, it divides the image into a number of self-similar boxes. Applying disjoint covering by boxes in an “up-scaling” partitioning process we obtain the partition function $\chi(q, \delta)$ (Feder, 1989) defined as:

$$\chi(q, \delta) = \sum_{i=1}^{N(\delta)} \mu_i^q(\delta) = \sum_{i=1}^{N(\delta)} m_i^q \quad (6)$$

where m is the mass of the measure, q is the mass exponent, δ is the length size of the box and $N(\delta)$ is the number of boxes in which $m_i > 0$. Based on this, the mass exponent function $\tau(q)$ shows how the moments of the measure scales with the box size:

$$\tau(q) = \lim_{\delta \rightarrow 0} \frac{\log \langle \chi(q, \delta) \rangle}{\log(\delta)} = \lim_{\delta \rightarrow 0} \frac{\log \langle \sum_{i=1}^{N(\delta)} m_i^q \rangle}{\log(\delta)} \quad (7)$$

where $\langle \rangle$ represents statistical moment of the measure $\mu_i(\delta)$ defined on a group of non overlapping boxes of the same size partitioning the area studied.

The singularity index, α , can be determined by the Legendre transformation of the $\tau(q)$ curve (Halsey, 1986) as:

$$\alpha(q) = \frac{d\tau(q)}{dq} \quad (8)$$

The number of cells of size δ with the same α , $N_\alpha(\delta)$, is related to the cell size as $N_\alpha(\delta) \propto \delta^{-f(\alpha)}$, where $f(\alpha)$ is a scaling exponent of the cells with common α . Parameter $f(\alpha)$ can be calculated as:

$$f(\alpha) = q\alpha(q) - \tau(q) \quad (9)$$

Multifractal spectrum (MFS) shown as plot of α vs. $f(\alpha)$, quantitatively characterizes variability of the measure studied with asymmetry to the right and left indicating domination of small and large values respectively (Evertsz and Mandelbrot, 1992). There are three characteristic values obtained from MFS, the singularity $\alpha(q)$ values for $q = \{0, 1, 2\}$. The first value ($\alpha(0)$) corresponds to the maximum of MFS and it is related to the box-counting dimension of the measure support; the second value is related to information or entropy dimension ($\alpha(1)$) and the third with the correlation dimension. The entropy dimension quantifies the degree of disorder present in a distribution. According to Andraud et al. (1994) and Gouyet (1996) a $\alpha(1)$ value close to 2.0 characterizes a system uniformly distributed throughout all scales, whereas a $\alpha(1)$ close to 0 reflects a subset of the scale in which the irregularities are concentrated. These three values will be shown from each calculation of MFS.

The width of the MF spectrum (Δ) indicates overall variability (Tarquis et al., 2001; 2014) and we have split it in two sections. Section I correspond to values $\alpha(q) < \alpha(0)$ or $q > 0$ and

section II to values with $\alpha(q) > \alpha(0)$ or $q < 0$. In section I the amplitude, or semi-width, was calculated with differences $\Delta^+ = \alpha(0) - \alpha(+5)$, and in section II with $\Delta^- = \alpha(-5) - \alpha(0)$.

To study the asymmetry of the multifractal spectrum we have choose the asymmetry index (AI) estimated as (Xie et al., 2010):

$$AI = \frac{\Delta\alpha_L - \Delta\alpha_R}{\Delta\alpha_L + \Delta\alpha_R} \quad \begin{matrix} \Delta\alpha_L = \alpha_0 - \alpha_{min} \\ \Delta\alpha_R = \alpha_{max} - \alpha_0 \end{matrix} \quad (10)$$

In our case, α_0 is the singularity for $q=0$ or $\alpha(0)$, α_{min} is $\alpha(+5)$ and α_{max} is $\alpha(-5)$.

Therefore, we can rewrite AI as:

$$AI = \frac{\Delta^+ - \Delta^-}{\Delta^+ + \Delta^-} \quad (11)$$

Expressing AI as equation (11), we can see that it is a normalized index based on the amplitudes Δ^+ and Δ^- .

There are several works relating the UM model and the multifractal formalism based on $\tau(q)$ (Gagnon et al., 2003; Aguado et al., 2014; Morató et al., 2017 among others) through the equations:

$$f(\alpha) = E - c(\gamma); \quad \alpha = E - \gamma \quad (12)$$

$$\tau(q) = E(q - 1) - K(q) \quad (13)$$

where E is the Euclidean dimension where the measure is embedded, in this case will be $E=2$, and $c(\gamma)$ is the codimension of the singularity of the density of the multifractal measure γ .

3 Results and Discussion

3.1 Radiometric influence in the Multifractal spectrum

To study the influence of radiometric resolution on Ikonos-2 image information complexity, the original pixel code (11 bits) has been transform to 8 bits through a rescaling based on minimum and maximum values between 0 and 255, with the aim of preserving the initial histogram shape.

We first discuss the results obtained for the 2048 x 2048 pixels Ikonos-2 image shown in Fig. 1, in bands combination of false colour (IK#4, IK#3, IK#2 bands combination in RGB visualization). In Fig. 2 IK#1, IK#2, IK#3, IK#4 bands histograms are shown. In the right column are histograms with the original radiometric resolution and in the left column the corresponding histograms rescaled to 8 bits. The histograms present a bimodal structure with a narrow peak of low value pixels (dark grey) showing a sharp maximum and a wider peak around a second lower maximum. For bands IK#1, IK#2, IK#3 the narrow peak maximum corresponds to vegetation, mainly irrigate crops, showing strong water absorption. This effect is particularly important in band IK#3. High value pixels (lighter grey) correspond to ground zones with lower vegetation content. However, as vegetation shows high reflectivity in the near infrared, IK#4 band histogram shows a predominance of high values pixels (lighter grey pixels) corresponding to dense vegetation parts. For both radiometric resolutions the shapes of the histograms are very similar as it was our intention (see Fig. 2).

We cover the image with boxes of size $\delta = 2^{-n}$ and we change the box size from 2048 to 2 pixels, that is, $\delta = 2048 / 2^n$ with $n = 0, 1, 2, \dots, 10$. For each value of the parameter q , from -5 to +5 with increments of 0.5, the partition function (equation 6) is computed and $\log \chi(q, \delta)$ vs $\log \delta$ is plotted in Fig. 3. Each graph contains 11 points and from these a range of scales are selected for the least-square linear fit reaching the maximum possible scales and with a standard error in the slope, the estimated values of $\tau(q)$, less than 0.01. Then, using Eq. [7-8], $\alpha(q)$ and $f(\alpha)$ are obtained. Comparing the range of scales used in both radiometric resolutions, the bands using the original data (11 bits) showed a wider range of scales for the

linear fit, up to 4 pixels, whereas in the 8 bits radiometric resolution were required up to 32 pixels (see arrows in Fig. 3).

The MF spectra $f(\alpha)$ corresponding to the four bands of multispectral Ikonos' images are shown in Fig. 4. These differences found in the multiscaling behaviour of each band are in agreement with previous works (Cheng, 2004; Lovejoy et al., 2008). Just by visual observation, it is remarkable the difference in the bands #3 and #4, R and NIR respectively, between 8 and 11 bits. Higher radiometric resolution gives a higher range of possible grey values per pixel. Note that this radiometric resolution effect is manifested in both sections of the MF spectra (for $q > 0$ and for $q < 0$).

Some characteristic parameters obtained from these MF spectra are shown in Table 1 and Table 2. As expected, in both radiometric resolutions and in each band the $\alpha(0)$ is practically 2, as the measure is defined in the entire plane and it has an Euclidean dimension of 2. Respect to the $\alpha(1)$ value certain differences are found. Comparing the bands in 8bits to the same ones in 11bits always the entropy dimension was higher. However, considering the standard errors only IK#1 (B) and IK#2 (G) bands were significantly different showing the B band the highest difference. Meanwhile, R and NIR bands aren't significantly different. This point out that a more uniformly distribution in space for the bands of Ikonos-2 8bits than in 11bits. The same behaviour is observed in the $\alpha(2)$.

The amplitudes calculated (Δ^+ and Δ^-) in Ikonos-2 11bits bands presents opposite trends (Table 1). Note that amplitude Δ^+ decreases as bands wavelength grows whereas the other amplitude Δ^- diminishes. Observing these parameters in Ikonos-2 8bits bands (Table 2) a different trend and behaviour are found. In this case both Δ^+ and Δ^- increase as the

wavelength increases for the three visible bands, but decreasing for the near infrared band (IK#4).

The AI estimated on these MFS amplitudes on each radiometric resolution are showed in the last column of Table 1 and Table 2. Comparing the bands in 8bits to the same ones in 11bits the behaviour is similar; there is a decreasing trend from IK#1 to IK#4, although the range of values is different. At a resolution of 11bits from a positive $AI = 0.240$ at B band goes to a negative $AI = -0.237$ at NIR band. On the other hand, at a resolution of 8bits from an $AI = 0.092$ goes to a negative $AI = -0.347$. The MFS more symmetric are found in G and R bands at a resolution of 11bits and in B and G bands at a resolution of 8bits.

Doing the same study for the vegetation indexes we found the following. The bi-log plot of the partition function ($\chi(q, \delta)$) vs δ is plotted in Fig. 5 for both VI at both radiometric resolutions. Each graph contains 11 points as the bands from where they were estimated. The linear fit was done with the same methodology that for the four bands. In this case only EVI at 8bits show a better linear trend in a wider range of scales. However, to better compare both VIs, from both radiometric resolutions, a range achieving 32 pixels (128 m.) was selected as showed by arrows in Fig. 5.

The MF spectra $f(\alpha)$ of EVI and NDVI estimated for both radiometric resolutions of Ikonos' images are shown in Fig. 4. Both vegetation indexes show differences due to the transformation from 11bits to 8bits. However, NDVI shows higher differences in the MFS, mainly in the part corresponding to q negative values (right side). Even EVI presents changes; its MFS is closer at both radiometric resolutions. Comparing the range of $f(\alpha)$ values in the VIs to the range obtained in the four bands (left column in Fig. 4) there is a remarkable contrast. Meanwhile the NIR band of 8bits achieves $f(\alpha)$ value close to 0.5, EVI and NDVI achieve values closer to 0.2. These differences are higher in 11bits image; R band achieves a $f(\alpha)$ value close to 0.9 and VIs achieve again values around to 0.2. The same characteristic

parameters obtained from the bands MF spectra were calculated for the vegetation indexes and are shown in Table 1 and Table 2.

In respect to the $\alpha(1)$ values certain differences are found between the vegetation indexes. Comparing the NDVI in 8bits to the same ones in 11bits always the entropy dimension was higher as it was found in the bands. However, EVI shows the contrary, entropy values of 11bits image are higher than 8bits image, although the differences aren't significant. Therefore, the radiometric resolution is affecting more to NDVI than to EVI. The former presents a more uniformly space distribution in 8bits than in 11bits image. The same behaviour is observed in $\alpha(2)$.

The amplitudes calculated (Δ^+ and Δ^-) in Ikonos-2 11bits VIs presents a similar situation (Table 1). The amplitude Δ^+ is lower than amplitude Δ^- and therefore the AI estimated is negative. This is visually perceived in Fig. 4, right column. Observing these parameters in Ikonos-2 8bits vegetation indexes (Table 2) similar situation are found but the values are lower. In both images (11bits and 8bits) NDVI shower higher values for both amplitudes, Δ^+ and Δ^- .

All the AI estimated for both vegetation indexes on each radiometric resolution are negative (Table 1 and Table 2) indicating a high asymmetry on the right part of the MFS as showed in Fig. 4. Comparing the AI values in 8bits to the same ones in 11bits they are similar pointing out that the shape of the MFS is similar as this index is a normalized index. However the values of the amplitudes mark a higher change in NDVI than in EVI.

3.2 Spatial resolution influence in the Multifractal spectrum

A comparison between Landsat, with an original pixel code of 8 bits, and the rescaled histograms from Ikonos, with an original pixel code of 11 bits, is made. In this section, we discuss the results obtained in the MF analysis on 512 x 512 pixels Landsat-7 image shown in Fig. 6, in bands combination of false colour (ETM+#3, ETM+#2 and ETM+#1 bands combination in RGB visualization).

In the right column of Fig. 6, the histograms of the Landsat-7 image for the first four bands are showed. The histograms present a bimodal structure except for ETM+#4 (NIR) which there is only one peak. Comparing these histograms with the ones obtained for Ikonos-2 8bits (Fig. 2) the peaks aren't so abrupt and narrow. At the same time, ETM+#1, ETM+#2 and ETM+#3 bands show the absolute maximum peak at high value pixels (light grey) and a second one at lower value pixels (dark grey). These bands are more centred and don't show a shift to the left as the Ikonos-2 8bits bands (IK#1, IK#2 and IK#3. In the case of NIR band, Landsat-7 and Ikonos-2 8bits are quite similar except for the absence of a second peak.

In the calculations, box sizes range from 512 to 2 pixel, that is, $\delta = 512 / 2^n$ with $n = 0, 1, \dots, 8$. For each value of the parameters q , from -5 to +5 with increments of 0.5, we compute the partition function, and the bi-log $\chi(q, \delta)$ vs δ are plotted in Fig. 7. In this case each linear fits contains only 9 points as the size of the image is 512x512 pixels. The same method was applied to select the range of scales used in the linear fit, achieving a scale of 4 pixels. Changing from pixels to meters, the scale achieved used in Landsat-7, in the MF analysis, was around 120 m. In the case of Ikonos-2 8bits the scale was 32 pixels or 128 m, very close to Landsat-7.

The MF spectra, $f(\alpha)$, corresponding to the first four bands of multispectral Landsat-7 images are shown in Fig. 8. From a comparison of figures 4 and 8 we see that Landsat-7 images MF spectra are always located inside the corresponding Ikonos-2 MF spectra. For a given value of Hölder exponent α the relation $f_{Landsat}(\alpha) \leq f_{Ikonos}(\alpha)$ is always satisfied. This result means that Landsat-7 images show lower complexity than Ikonos-2 8bits images. As

1 stated in section 2.1 Ikonos-2 satellite data are coded in 11 bits in contrast with Landsat-7 8
2 bits coded data. To compare both sensors, with different spatial resolution, we pass Ikonos-2
3 from 11bits to 8bits observing that the later shows more complexity than Landsat.

4
5 The MF spectra parameters from Landsat-7 are shown in Table 3. We will compare in this
6 section with Ikonos-2 8bits (Table 2). The $\alpha(1)$ values from the four bands of Landsat-7 are
7 higher than the ones presented by Ikonos-2 8bits indicating a higher uniformity space
8 distribution. Comparing between the bands, there are not significant differences contrary with
9 the trend we observed among them in Ikonos-2 8bits. The $\alpha(2)$ shows the same behaviour.

10
11 The amplitudes calculated (Δ^+ and Δ^-) in Landsat-7 bands present few variations (Table 3).

12 The amplitude Δ^+ decreases from ETM+#1 to ETM+#3 and then presents an increase in
13 ETM+#4 (NIR) whereas the other amplitude Δ^- remain practically constant. Observing these
14 parameters in Ikonos-2 8bits bands (Table 2) there are variations in value and behaviour for
15 the four bands. In this case, both Δ^+ and Δ^- increase as the wavelength increases for the three
16 visible bands, but decreasing for the near infrared band (IK#4).

17
18 The AI estimated on these MFS amplitudes on each Landsat-7 bands are positive except for
19 ETM+#3 (R band). For the G band (ETM+#3) the symmetry of the MFS is complete. The
20 band that shows certain asymmetry is the B band (ETM+#1).

21
22 Regarding the vegetation indexes, estimated on Landsat-7 bands, we found the following. The
23 bi-log plot of the partition function ($\chi(q, \delta)$) vs δ is plotted in Fig. 9 for both VIs. Each graph
24 contains 9 points as the bands from where they were estimated. The linear fit was done with
25 the same methodology that for the four bands. EVI and NDVI show the same behaviour and
26 the same range of scale was selected achieving 8 pixels as showed by arrows in Fig. 9.

The MF spectra $f(\alpha)$ of EVI and NDVI estimated based on Landsat-7 image are shown in Fig. 8. Both vegetation indexes show differences mainly in the right side of the MFS (for q negative values). Comparing the range of $f(\alpha)$ values in the VIs to the range obtained in the four bands (left column in Fig. 8) there is a remarkable contrast. Meanwhile the NIR band of 8bits achieves $f(\alpha)$ value close to 1.6, EVI and NDVI achieve values closer to 1. A similar situation was found with both images of Ikonos-2.

We are going to study the parameters obtained from the MF spectra for the vegetation indexes (Table 3). The results are quite similar to those commented about the Landsat-7 bands showing even higher values, 1.996 NDVI and 1.997 EVI.

The amplitude Δ^+ is quite low compared with the bands and to the VIs of Ikonos-2 8bits. On the other hand, the amplitude Δ^- is higher than Landsat-7 bands but only a third of the values showed by Ikonos-2 8bits VIs (Table 2). The AI estimated for both vegetation indexes are negative indicating a high asymmetry on the right part of the MFS as showed in Fig. 8. Comparing the AI values of Landsat-7 VIs with the ones of both Ikonos-2 images, these are the highest indicating that show the most unbalance MFS shifted totally on the right side of the spectrum.

4 Conclusions

In this work, we have used MF spectra as a successful technique for analyzing common information contained in multi-spectral images of the site of the Earth surface acquired by two satellites, Landsat-7 and Ikonos, in four common bands in the visible (Blue, Green and Red) and near-infrared (NIR) wavelength regions used in several vegetation indexes.

1 The radiometric resolution has been studied comparing MF spectra of the images acquired by
2 Ikonos-2 coded in 11 bits and transformed in 8 bits code. The results obtained after the
3 histogram transformation in the blue and green bands were the ones you would expected after
4 the simplification applied from 11 to 8 bits, i.e. higher frequency in all the histogram bin
5 values (see Fig. 2). In contrast, red and infrared bands showed no sensitivity at all to this
6 transformation keeping similar MF spectra. To our knowledge, this is the first time these
7 differences among bands are reported.

8
9 In order to analyse the effect of spatial resolution in each band at 4 m (Ikonos-2 with 8 bits)
10 pixel size and 30 m (Landsat-7 with 8 bits) pixel size are compared. Obviously, the higher the
11 spatial resolution, the higher the Hölder spectrum amplitude in the green and blue bands are.
12 In fact, observing the graphics of the three cases studied (Ikonos-2 11 bits, Ikonos-2 8 bits and
13 Landsat-7 8 bits) both bands gradually reduce their $\alpha(q)$ amplitude in the negative as well as
14 in the positive q values. However, this is not the case for R and NIR bands that present a
15 much higher difference between Ikonos-2 8bits and Landsat-7 curves of the MF spectra than
16 between Ikonos-2 11bits and 8bits.

17
18 In the $q > 0$ MFS region for B and G bands the sensitivity to both factors are very similar,
19 being the B band ratio slightly higher. In the other two bands, R and NIR, for the same region
20 mainly present sensitivity to spatial resolution, showing a similar rate than blue and green
21 bands. Observing the $q < 0$ region for blue and green the behaviour is similar to the positive
22 one but with a lower ratio (between 1 and 2) and once more, the red and infrared bands show
23 slightly sensitivity to radiometric resolution. Nevertheless in the spatial resolution the R band
24 has a ratio similar to B and G, and NIR shows the highest ratio (around 8) pointing the
25 extreme influence of the lowest values contained, see histograms in Fig. 2 (Ikonos-2 8 and 11
26 bits) and Fig. 6 (Landsat-7).

27
28 The implications of these variations in the B, R and NIR in the multi-scaling behaviour of two
29 vegetation indexes, NDVI and EVI, have been also studied. The radiometric resolution
30 showed a higher influence in the MFS of the NDVI than in EVI. This implies that the use of

1 the B band in the later has a steady effect in the scaling behaviour. As commented for the
2 bands, the spatial resolution had a major impact in both vegetation indexes.

3
4 Further research will be conducted to establish a qualitative and quantitative comparison of
5 these conclusions among several multifractal methodologies applied on these images.

6 7 **Acknowledgements**

8 Thanks are due to the anonymous referees and the editor for their interest and patient in this
9 work. Discussion and comments suggested by Prof. Jose Manuel Redondo are highly
10 appreciated. This work has been supported by the Ministerio de Economía y Competitividad
11 (MINECO) under Contract Nos. MTM2012-39101 and MTM2015-63914-P.

References

- Andraud C, Beghdadi A and Lafait J (1994) Entropic analysis of morphologies. *Physica A* **207**, 208–212.
- Aguado, P.L., Del Monte, J.P., Moratiel, R., Tarquis, A.M., 2014. Spatial Characterization of Landscapes through Multifractal Analysis of DEM. *The Scientific World Journal*. Vol 2014. Article ID 563038, 9p. <http://dx.doi.org/10.1155/2014/563038>.
- Beaulieu, A. and Gaonac'h, H.: Scaling of differentially eroded surfaces in the drainage network of the Ethiopian plateau, *Rem. Sens. Environ.*, 82, 111–122, 2002.
- Ben-Ze'ev, E., Karnieli, A., Agam, N., Kaufman, Y., Holben, B., Assessing Vegetation Condition In The Presence Of Biomass Burning Smoke By Applying The Aerosol-Free Vegetation Index (AFRI) On MODIS Images, *International journal of remote sensing*, 27, 3203-3221, 2006.
- Carlson, T. N., and Ripley, D. A. On the relation between NDVI, Fractional Vegetation Cover, and Leaf Area Index. *Remote Sensing of Environment*, 62: 241–252. 1997.
- Cheng, Q. and Agterberg, F.P.: Multifractal modelling and spatial statistics. *Mathematical Geology*, 28(1), 1-16, 1996.
- Cheng, Q.: A new model for quantifying anisotropic scale invariance and for decomposition of mixing patterns, *Mathematical Geology*, 36, 345–360, 2004.
- De Cola, L., Fractal analysis of a classified Landsat-7 scene. *Photogrammetric Engineering and Remote Sensing* **55**(5). 1989.
- Deng, FP, Su, GL, Liu, C, Seasonal Variation Of MODIS Vegetation Indexes And Their Statistical Relationship With Climate Over The Subtropic Evergreen Forest In Zhejiang, China, *IEEE GEOSCIENCE AND REMOTE SENSING LETTERS*, 4, 236-240, 2007.
- Dial, G., Bowen, H., Gerlach, F., Grodecki, J. and Oleszczuk, R., IKONOS satellite, imagery and products. *Remote Sensing of Environment* **88**, 23-36. 2003.
- Du, G. and T.S. Yeo. A novel multifractal estimation method and its application to remote image segmentation. *IEEE Transactions on Geoscience and Remote Sensing* **40**(4), 980-982. 2002.

- 1 Evertsz, C.J.G., Mandelbrot, B.B.. In *Chaos and Fractals: New Frontiers of Science*, Peitgen,
2 H., Jurgens, H. and Saupe Springer-Verlag D., Eds., New York, 921. 1992.
- 3 Feder, J. *Fractals*. Plenum Press, New York, 283pp., 1988.
- 4 Fioravanti, S., *Multifractals: theory and application to image texture recognition*. In “Fractals
5 in Geosciences and Remote Sensing”, Proceedings of a joint JRC/EARSeL Expert meeting.
6 Ispra. Italy, 14 – 15 April 1994.
- 7 Gagnon, J.S., Lovejoy, S., Schertzer, D., 2003. Multifractal surfaces and terrestrial
8 topography. *Europhys. Lett.* 62, 801-807.
- 9 Gaonac’h, H., Lovejoy, S., and Schertzer, D.: Resolution dependence of infrared imagery of
10 active thermal features at Kilauea volcano. *Int. J. Rem.Sens.*, 24, 2323-2324, 2003.
- 11 Gouyet JF ((1996) *Physics and fractal structures*. (Springer-Verlag: New York)
- 12 Halsey, T.C., Jensen, M.H., Kadanoff, L.P., Procaccia, I. and Shraiman, B.I.. Fractal measures
13 and their singularities: the characterization of strange sets. *Phys. Rev. A* **33**, 1141-1151. 1986.
- 14 Harvey, D.C., Gaonac’h, H., Lovejoy, S. and Schertzer, D. : Multifractal characterization of
15 remotely sensed volcanic features: a case study from Kilauea volcano, Hawaii, *Fractals*, 10,
16 265-274, 2002.
- 17 Hirata, T. and Imoto, M., *Multifractal analysis of spatial distribution of micro-earthquakes in
18 the Kanto region*, *Geophys. J. Int.* **107**. 1991.
- 19 Huete, A., Miura, T., Yoshioka, H., Ratana, P. and Broich, M., *Indices of Vegetation Activity*
20 in “Biophysical Applications of Satellite Remote Sensing”. Jonathan M. Hanes Editor,
21 Springer, 2014.
- 22 Kravchenko, A.N., Boast, C.W. and Bullock, D.G., *Multifractal analysis of soil spatial
23 variability*, *Agron. J.* **91**. 1999.
- 24 Laferrière, A. and Gaonac’h, H.: Multifractal properties of visible reflectance fields from
25 basaltic volcanoes, *J.Geophys.Res.*, 104(B3), 5115-5126, 1999.
- 26 Lam, N.S. and De Cola, L., *Fractals in Geography*, Prentice Hall, Englewood Cliffs, New
27 Jersey. 1993.
- 28 Lam, N.S., *Description and measurement of Landsat-7 TM images using fractals*.
29 *Photogrammetric Engineering and Remote Sensing* **56**(2), 1990.

1 Lavallée, D., Schertzer, D., Lovejoy, S., 1991. On the determination of the codimension
2 function. In Schertzer, D., Lovejoy, S., (Eds.), *Non-Linear Variability in Geophysics*,
3 Springer Netherlands: Dordrecht, The Netherlands. pp. 99–109.

4 Lovejoy, S., Pecknold, S., and Schertzer, D.: Stratified multifractal magnetization and surface
5 geomagnetic fields-I. Spectral analysis and modelling, *Geophys. J. Int.*, 145, 112–126, 2001a.

6 Lovejoy, S., Schertzer, D., Tessier, Y. and Gaonach, H.: Multifractals and resolution-
7 independent remote sensing algorithms: the example of ocean colour. *Int. J. Remote Sensing*,
8 22(7), 119-1234, 2001b.

9 Lovejoy, S., Tarquis, A., Gaonach, H. and Schertzer, D.: Single and multiscale remote
10 sensing techniques, multifractals and MODIS derived vegetation and soil moisture, *Vadose*
11 *Zone J.*, 7, 533-546, 2008, doi: doi 10.2136/vzj2007.0173.

12 Maître, H. and Pinciroli, M.: Fractal characterization of a hydrological basin using SAR
13 satellite images, *IEEE Trans. Geosci. Rem. Sens.*, 37, 175–181, 1999.

14 Mandelbrot, B. B. *The Fractal Geometry of Nature*, Freeman, San Francisco. 1983.

15 Mao-Gui Hu, Jin-Feng Wang,* and Yong Ge. Super-Resolution Reconstruction of Remote
16 Sensing Images Using Multifractal Analysis. *Sensors (Basel)*, 9(11), 8669–8683, 2009. doi:
17 10.3390/s91108669

18 Mika, A.M., Three decades of Landsat-7 instruments. *Photogrammetric Engineering and*
19 *Remote Sensing* **63**, 839-852. 1997.

20 Morató, M.C., Castellanos, M.T., Bird, N.R., Tarquis, A.M.: Multifractal analysis in soil
21 properties: Spatial signal versus mass distribution. *Geoderma*, 287, 54-65, 2017.
22 <http://dx.doi.org/10.1016/j.geoderma.2016.08.004>.

23 Parrinello, T. and R.A. Vaughan. Multifractal Analysis and feature extraction in satellite
24 imagery. *Int. J. of Remote Sensing* **23**(9), 1799-1825. 2002.

25 Plotnick R.E., Gardner, R.H., Hargrove, W.W., Prestegard, K., Perlmutter, M.. Lacunarity
26 analysis: a general technique for the analysis of spatial patterns. *Phys. Rev. E.* 53(5), 5461-
27 5468. 1996.

28 Qiu, H., Lam, N.S., Quattrochi, D.A. and Gamon, J.A., *Fractal characterization of*
29 *hyperspectral imagery*, *Photogrammetric Engineering and Remote Sensing* **65**(1). 1999.

Renosh, P. R., Schmitt, F. G., and Loisel, H.: Scaling analysis of ocean surface turbulent heterogeneities from satellite remote sensing: use of 2D structure functions. PLoS ONE, 10, e0126975, 2015. doi:10.1371/journal.pone.0126975.

Sánchez, A., Serna, R., Catalina, F. and Afonso, C.N., *Multifractal patterns formed by laser irradiation in GeAl thin multilayer films*, Physical Review B, **46**(1). 1992.

Schertzer, D., Lovejoy, S. 1987. Physical modeling and analysis of rain and clouds by anisotropic scaling multiplicative processes. J. Geophys. Res. 92, 9693–9714.

Schmitt, F., Schertzer, D., Lovejoy, S., and Marchal, P.: Multifractal analysis of satellite images: towards an automatic segmentation. In *Fractals in Engineering* (Arcachon: Jules), 103-109, 1997.

Tarquis, A.M., Platonov, A., Matulka, A., Grau, J., Sekula, E., Diez, M. and Redondo J. M. Application of multifractal analysis to the study of SAR features and oil spills on the ocean surface. Nonlin. Processes Geophys., 21, 439-450, 2014.

Tarquis, A.M., Giménez, D., Saa, A., Díaz, M.C. and Gascó, J.M., *Scaling and multiscaling of soil pore systems determined by image analysis*, in “Scaling methods in soil physics”. Ed. Y. Pachepsky, D.E. Radcliffe and H. Magdi Selim. CRC Press. 2003.

Tarquis, A.M., Losada, J.C., Benito, R. and Borondo, F., Multifractal analysis of the Tori destruction in a molecular Hamiltonian System. Phys. Rev. E. **65**, 0126213(9). 2001.

Tessier, Y., Lovejoy, S., Schertzer, D., Lavalley'e, D., and Kerman, B.: Universal multifractal indices for the ocean surface at far red wavelengths. Geophysical Research Letters, 20, 1167-1170, 1993.

Turiel, A., Isern-Fontanet, J., García-Ladona, E. and Font, J., Multifractal Method for the Instantaneous Evaluation of the Stream Function in Geophysics Flows. Phys. Rev. Lett. **95**, 104502. 2005.

Wang, X., Xie, H., Guan, H., and Xiaobing, Z, Different responses of MODIS-derived NDVI to root-zone soil moisture in semi-arid and humid regions, Journal of Hydrology, 340, 12– 24, 2007.

Xie, S., Q. Cheng, X. Xing, Z. Bao, and Z. Chen. Geochemical multifractal distribution patterns in sediments from ordered streams. Geoderma, 160, 36-46, 2010.

Table 1. Parameters obtained from the multifractal spectrum from each band of Ikonos-2 image, and the vegetation indexes (VI) estimated, with a pixel size of 4 m and a radiometric resolution of 11 bits. . The amplitudes of α values are presented as Δ^+ and Δ^- corresponding to $\alpha(0)$ - $\alpha(5)$ and $\alpha(-5)$ - $\alpha(0)$ respectively. And the asymmetry index (AI) corresponding to

$$\frac{\Delta^+ - \Delta^-}{\Delta^+ + \Delta^-}$$

Ikonos-2 (11bits)	Band	q	$\alpha(q)$	Δ^+	Δ^-	AI
	IK#1	0	2.001 \pm 0.001	0.418	0.256	0.240
		1	1.938 \pm 0.005			
		2	1.865 \pm 0.009			
	IK#2	0	2.001 \pm 0.001	0.377	0.313	0.093
		1	1.936 \pm 0.005			
		2	1.871 \pm 0.007			
	IK#3	0	2.001 \pm 0.001	0.348	0.382	-0.047
		1	1.937 \pm 0.005			
		2	1.878 \pm 0.006			
	IK#4	0	2.001 \pm 0.001	0.290	0.470	-0.237
		1	1.959 \pm 0.005			
		2	1.908 \pm 0.009			

Ikonos-2 (11bits)	VI	q	$\alpha(q)$	Δ^+	Δ^-	AI
	NDVI	0	2.000 \pm 0.001	0.516	1.166	-0.386
		1	1.886 \pm 0.008			
		2	1.779 \pm 0.010			
	EVI	0	2.000 \pm 0.001	0.270	0.877	-0.533
		1	1.948 \pm 0.002			
		2	1.897 \pm 0.004			

Table 2. Parameters obtained from the multifractal spectrum from each band of Ikonos-2 image, and the vegetation indexes (VI) estimated, with a pixel size of 4 m and a radiometric resolution of 8 bits. The amplitudes of α values are presented as Δ^+ and Δ^- corresponding to $\alpha(0)$ - $\alpha(5)$ and $\alpha(-5)$ - $\alpha(0)$ respectively. And the asymmetry index (AI) corresponding to

$$\frac{\Delta^+ - \Delta^-}{\Delta^+ + \Delta^-}.$$

Ikonos-2 (8bits)	Band	q	$\alpha(q)$	Δ^+	Δ^-	AI
	IK#1	0	2.000±0.001	0.231	0.192	0.092
		1	1.971±0.003			
		2	1.930±0.006			
	IK#2	0	2.000±0.001	0.270	0.287	-0.031
		1	1.963±0.004			
		2	1.914±0.006			
	IK#3	0	2.000±0.001	0.323	0.614	-0.311
		1	1.945±0.005			
		2	1.887±0.006			
	IK#4	0	2.000±0.001	0.248	0.512	-0.347
		1	1.966±0.004			
		2	1.923±0.008			

Ikonos-2 (8bits)	VI	q	$\alpha(q)$	Δ^+	Δ^-	AI
	NDVI	0	2.000±0.002	0.337	0.984	-0.490
		1	1.932±0.005			
		2	1.855±0.008			
	EVI	0	2.000±0.002	0.300	0.874	-0.488
		1	1.940±0.004			
		2	1.873±0.006			

Table 3. Parameters obtained from the multifractal spectrum from each band of Landsat-7 image, and the vegetation indexes (VI) estimated, with a pixel size of 4 m and a radiometric resolution of 8 bits. The amplitudes of α values are presented as Δ^+ and Δ^- corresponding to $\alpha(0)-\alpha(5)$ and $\alpha(-5)-\alpha(0)$ respectively. And the asymmetry index (AI) corresponding to

$$\frac{\Delta^+ - \Delta^-}{\Delta^+ + \Delta^-}$$

Landsat-7	Band	q	$\alpha(q)$	Δ^+	Δ^-	AI
	ETM+#1	0	2.001±0.001	0.160	0.119	0.147
		1	1.985±0.005			
		2	1.960±0.010			
	ETM+#2	0	2.003±0.001	0.119	0.119	0.000
		1	1.988±0.004			
		2	1.970±0.008			
	ETM+#3	0	2.001±0.001	0.095	0.110	-0.073
		1	1.989±0.004			
		2	1.974±0.007			
	ETM+#4	0	2.017±0.001	0.106	0.104	0.010
		1	1.989±0.004			
		2	1.973±0.008			

Landsat-7	VI	q	$\alpha(q)$	Δ^+	Δ^-	AI
	NDVI	0	2.001±0.001	0.028	0.353	-0.852
		1	1.996±0.001			
		2	1.992±0.001			
	EVI	0	2.001±0.001	0.022	0.288	-0.859
		1	1.997±0.001			
		2	1.994±0.001			



Figure 1. The Ikonos-2 image in band combinations of false colour (IK#4, IK#3 and IK#2 in RGB). The image has a size of 2048 x 2048 pixels, each area unit correspond to 4x4 m. The coordinates UTM (zone 30) of the upper left and low right pixel in the image are: ULX = 446037 m, ULY = 4441684 m, LRX = 454229 m and LRY = 4433492 m.

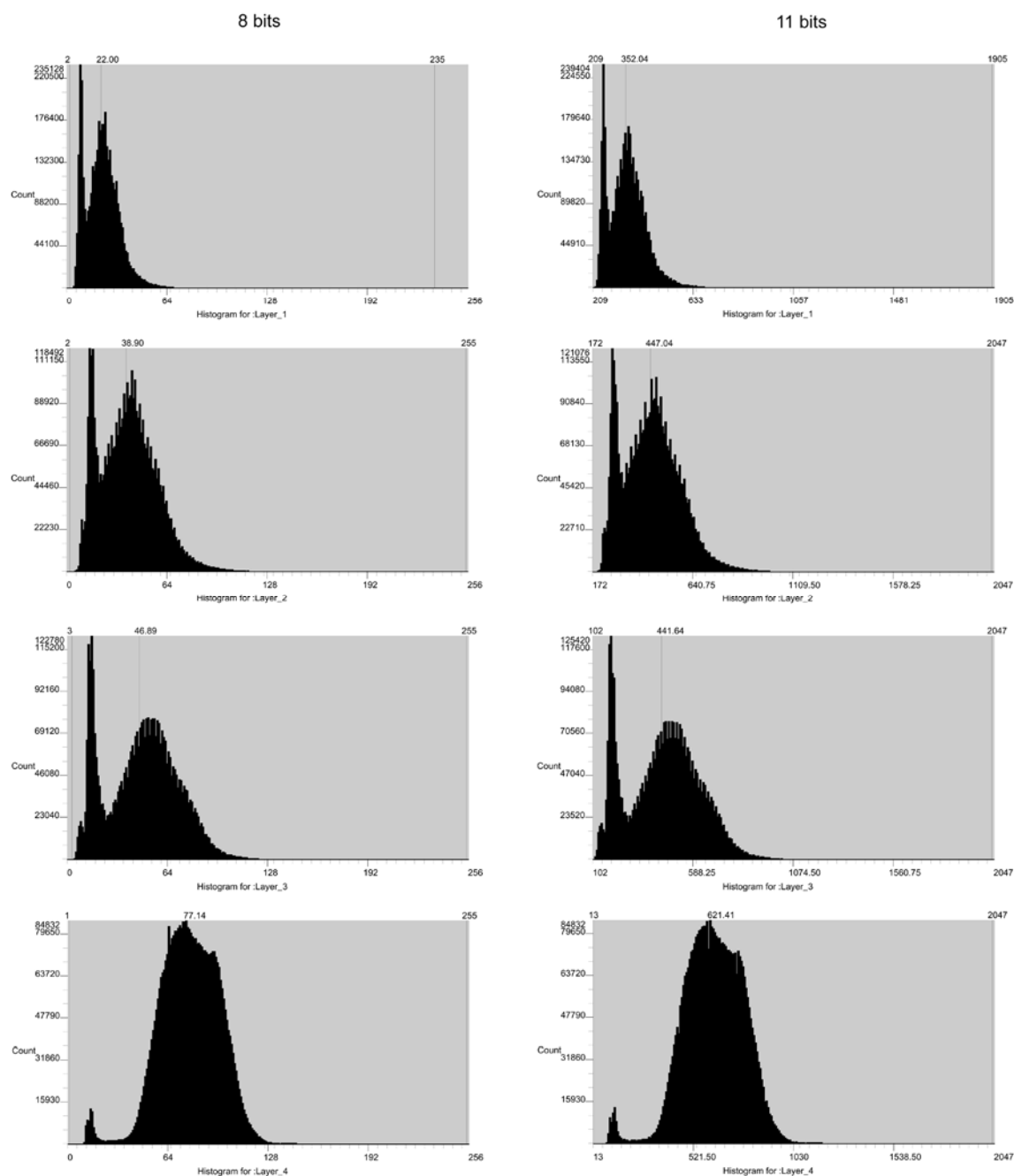


Figure 2. Histograms of the four bands of Ikonos-2 image for the original radiometric resolution, 11 bits (right), and the minimum-maximum rescale 8 bits radiometric resolution (left).

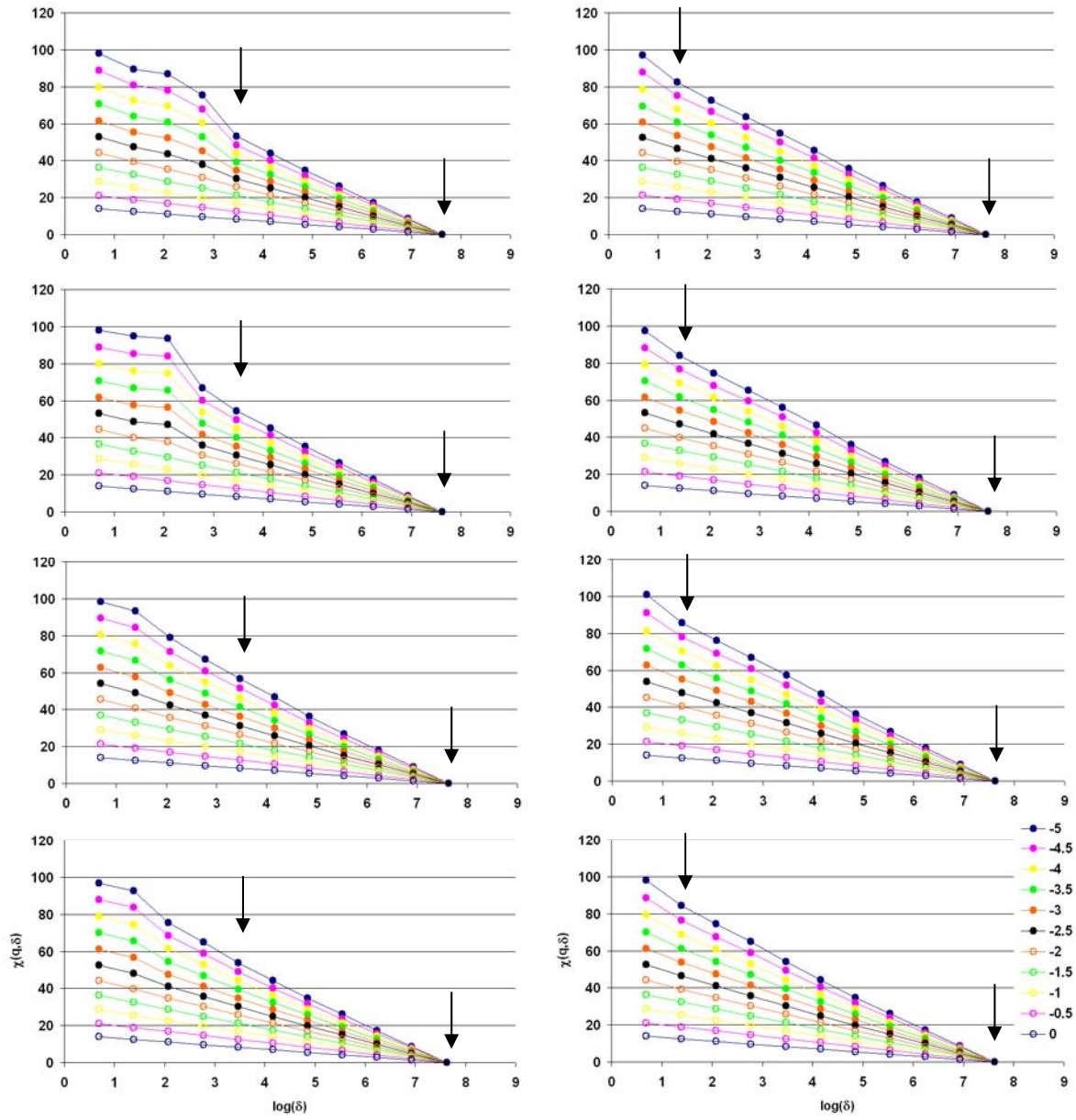
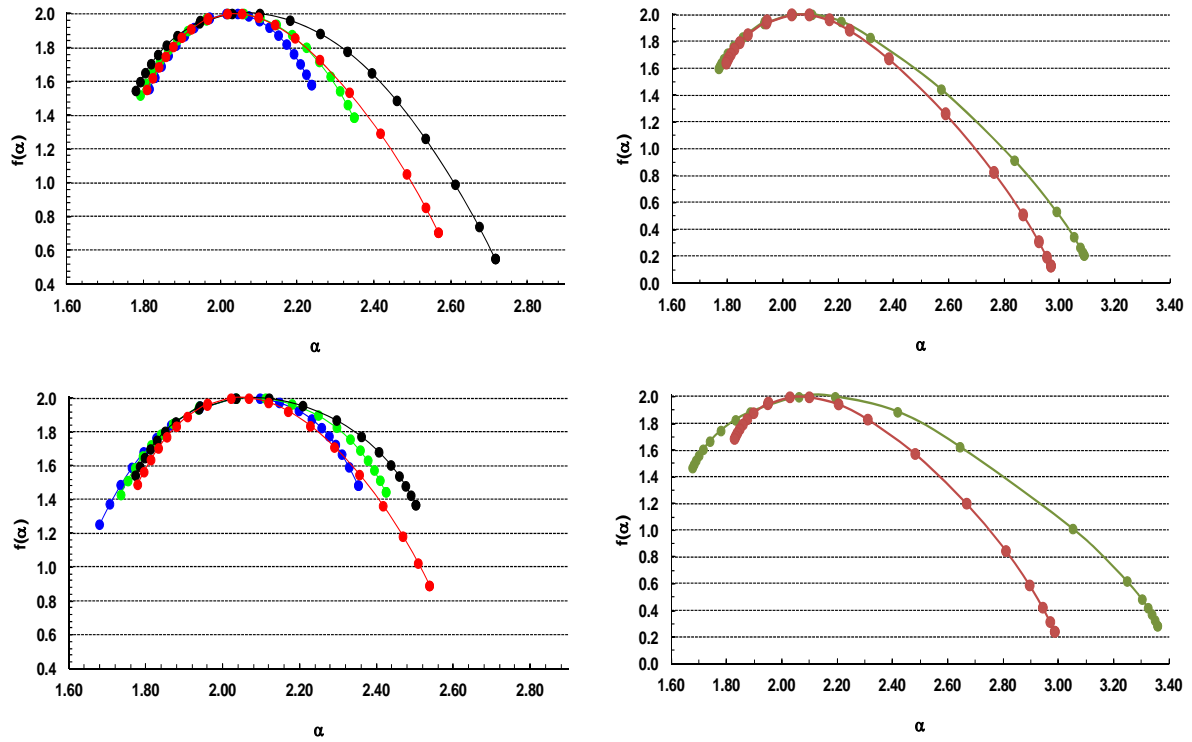


Figure 3. Bi-log plots of the partition function $\chi(q, \delta)$ versus δ for the first four bands of Ikonos-2 satellite and for $q < 0$ values. From top to bottom we show the results for IK#1, IK#2, IK#3 and IK#4. The left column correspond to 8-bits image and the right column to 11 bits image. The arrows marked the range of scales used for the fit and to calculate the slope for different values of q (7 points in the left column and 10 points in the right column).

1



2

3 Figure 4. Multifractal spectrum of Ikonos-2 images for the original pixel values coded in 11
 4 bits (lower) and the min-max rescale to 8 bits (upper). Left column correspond to each band
 5 analyzed: IK#1 in blue colour, IK#2 in green colour, IK#3 in red colour and IK#4 in black.
 6 Right column correspond to vegetation indexes: NDVI in green colour and EVI in brown.

7

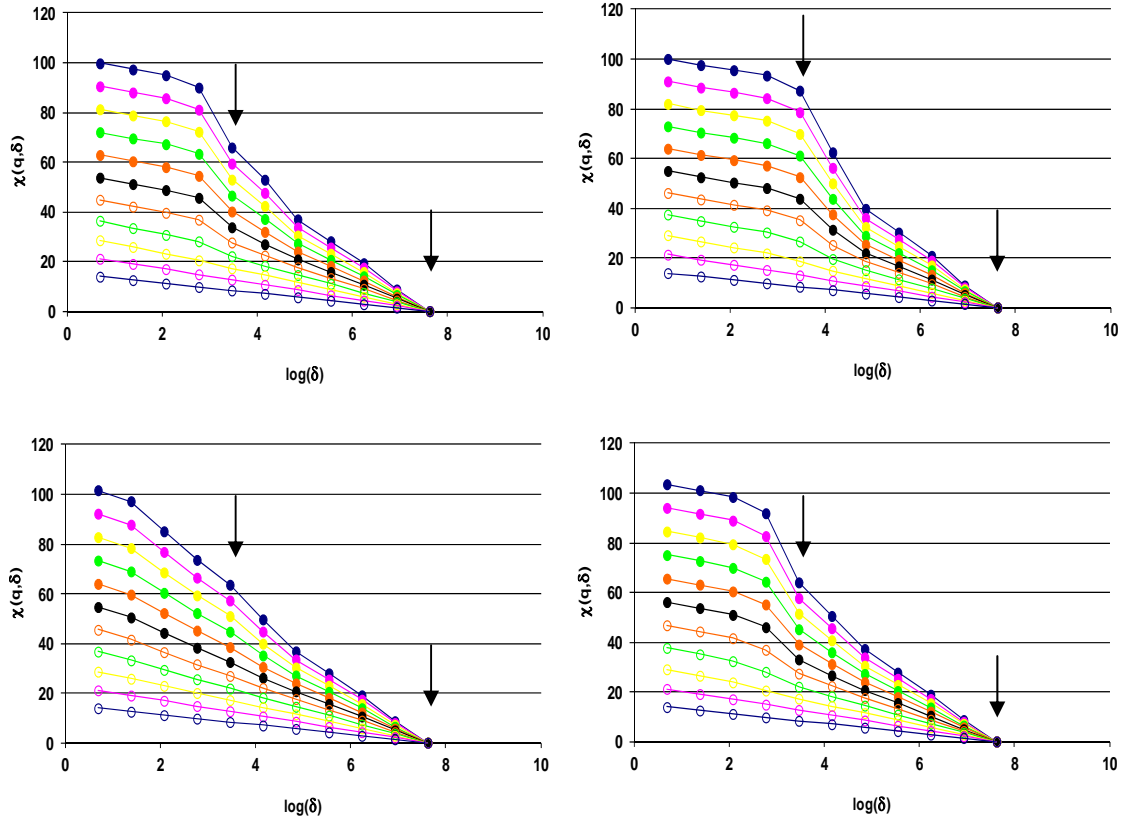
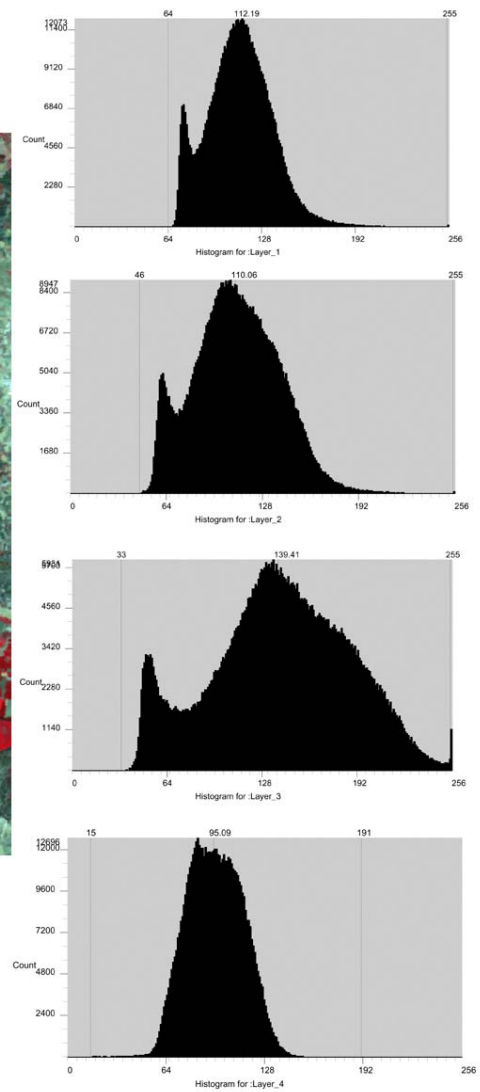
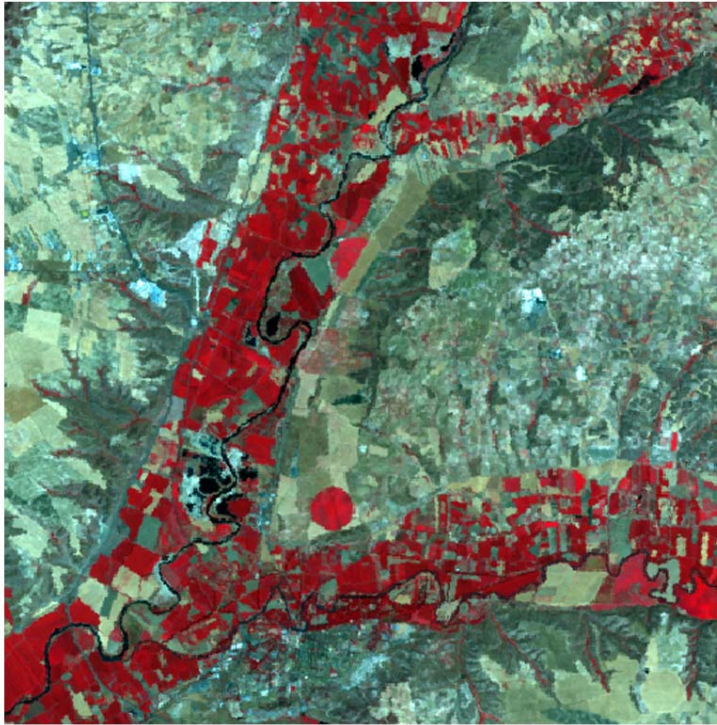


Figure 5. Bi-log plots of the partition function $\chi(q, \delta)$ versus δ for the vegetation indexes estimated from B, R and NIR bands of Ikonos-2 satellite and for $q < 0$ values. From top to bottom we show the results for NDVI and EVI respectively. The left column correspond to 8-bits image and the right column to 11 bits image. The arrows marked the range of scales used for the fit and to calculate the slope for different values of q (7 points).

1



2

3 **Figure 6.** The Landsat-7 image and the histograms for the first four bands: blue (ETM+ #1),
 4 green (ETM+ #2), red (ETM+ #3) and near infrared (ETM+ #4). The image has a size of
 5 **512x512 pixels**, each area unit correspond to 30x30 m. The coordinates UTM (zone 30) of the
 6 upper left and low right pixel in the image are: **ULX = 442185 m, ULY = 4445568 m, LRX =**
 7 **457545 m and LRY = 4430208 m.**

8

9

10

11

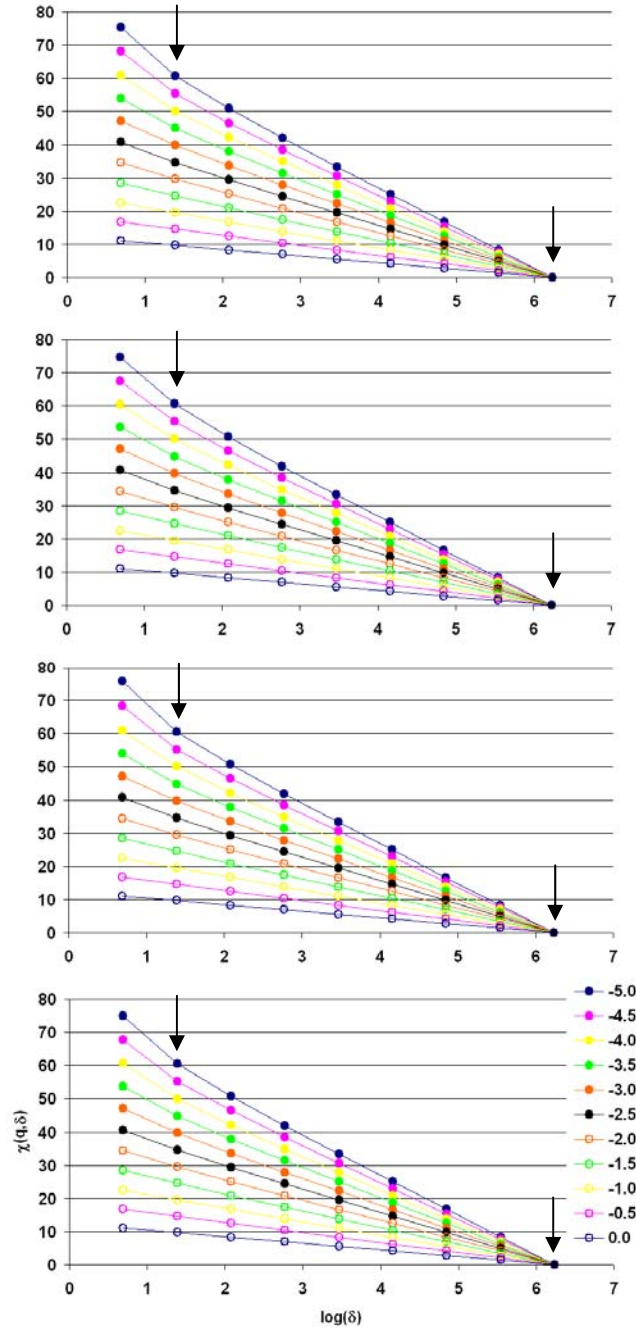
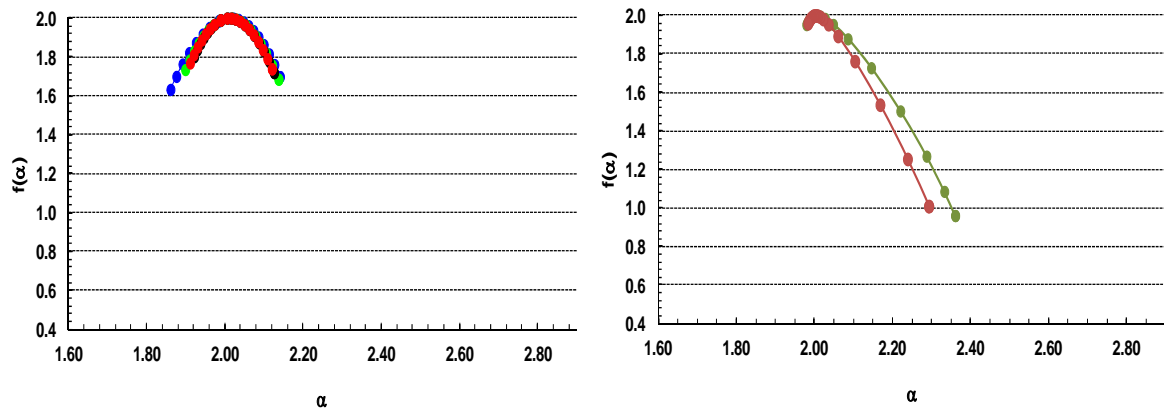


Figure 7. Bi-log plots of the partition function $\chi(q, \delta)$ versus δ for the first four bands of Landsat-7 satellite and for $q < 0$ values. From top to bottom we show the results for ETM+#1, ETM+#2, ETM+#3 and ETM+#4. The arrows marked the range of scales used for the fit and to calculate the slope for different values of q (8 points).

1
2

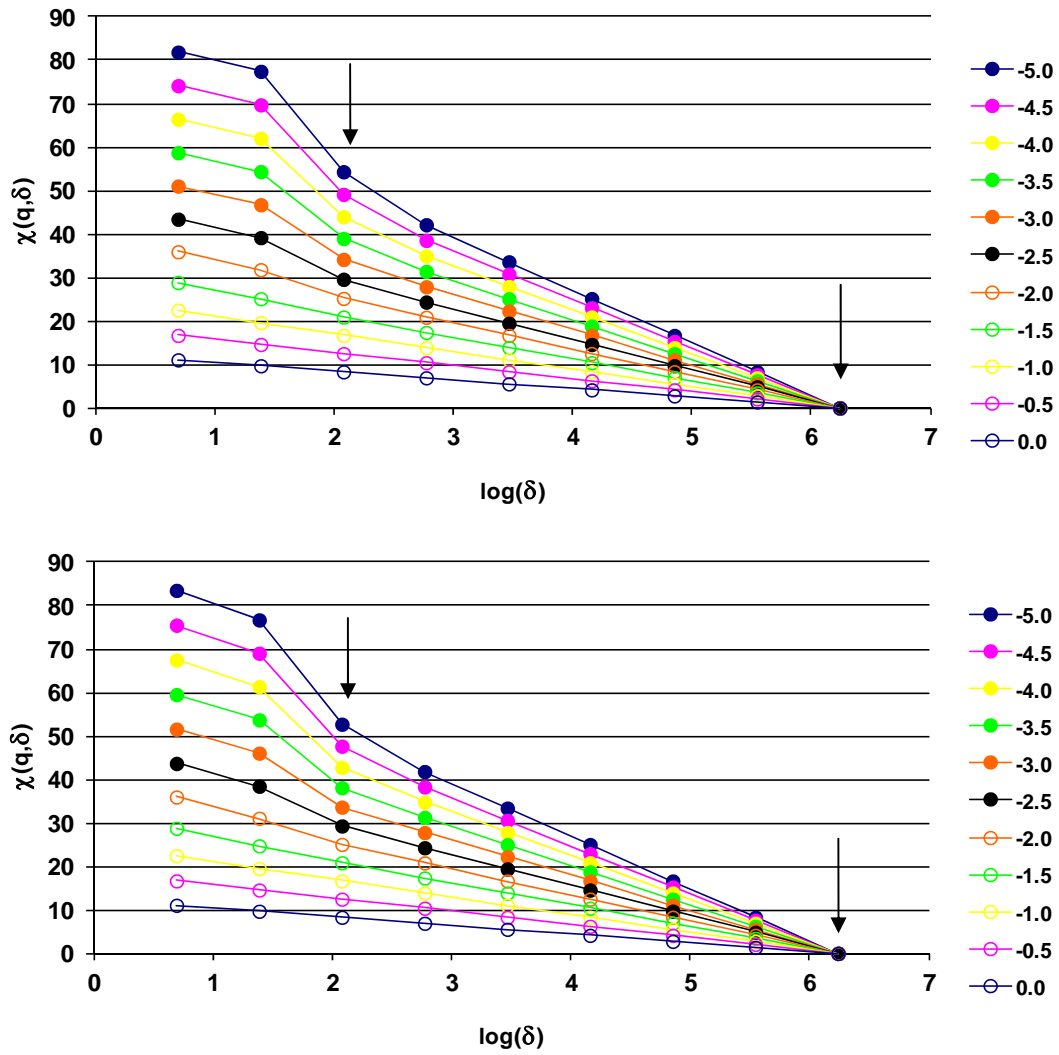


3

4 **Figure 8.** Multifractal spectrum of Landsat-7 image for the original pixel values coded in 8
5 bits. **Left plot correspond to each** band analyzed: ETM+#1 in blue colour, ETM+#2 in green
6 colour, ETM+#3 in red colour and ETM+#4 in black. **Right plot correspond to vegetation**
7 **indexes: NDVI in green colour and EVI in brown.**

8

1
2



3

4 Figure 9. Bi-log plots of the partition function $\chi(q, \delta)$ versus δ for the vegetation indexes
5 estimated from B, R and NIR bands of Landsat-7 satellite and for $q < 0$ values. From top to
6 bottom we show the results for NDVI and EVI. The arrows marked the range of scales used
7 for the fit and to calculate the slope for different values of q (7 points).